PART REMANUFACTURING USING HYBIRD MANUFACTURING PROCESSES

Xinchang Zhang and Frank Liou

Department of Mechanical and Aerospace Engineering
Missouri University of Science and Technology, Rolla, MO 65409

Abstract

Many users of high-performance metal parts, such as the aerospace industry, the mold/die casting industry, and heavy machinery consumers, extend the service of these damaged parts by employing remanufacturing technology. Additive manufacturing has unique capabilities, such as low heat input, a small heat-affected zone, free-form fabrication, and a near-net-shape. This paper summarizes the effort and the tested results to achieve an automated remanufacturing process using hybrid additive manufacturing and CNC machining processes. It will enable the robust remanufacturing-on-demand to significantly increase operational availability to reduce sustainment costs, thus will lead to robust and quality remanufacturing that is critical for remanufacturing process qualification.

Keywords: Remanufacturing; Hybrid processes; Direct laser deposition; Component repair

Introduction

Remanufacturing is an emerging industry, due to its benefits in cost- and energy-savings. Among various remanufacturing or repair processes, metal part remanufacturing plays an important role in the remanufacturing industry. Traditional remanufacturing processes rely on welding or brazing for material addition. Both of these processes induce a large HAZ (Heat Affected Zone) which can be detrimental to the final part's performance and life. The Direct Laser Deposition (DLD) process is a process which directly fabricates a fully dense metal part without intermediate steps and introduces a much smaller HAZ due to the usage of a high-density laser power. This process has been reported to be used in the repair of Integrally Bladed Rotors (IBR) [1]. Remanufacturing of costly metallic components (e.g. Titanium aircraft parts or high-precision die/mold) is crucial for maximizing service life to reduce costs of replacement [2]. However, lack of automation results in much higher remanufacturing cost, and introduces inconsistencies in remanufacturing quality, which dramatically reduces the lifetime of the restored parts. These drawbacks have significantly limited the application of metal remanufacturing technology.

Among categories of AM technologies according to ASTM F42, Directed Energy Deposition (DED) which covers a range of terminologies such as direct metal deposition, laser engineered net shaping and laser cladding is appropriate for remanufacturing high-value complex components that need frequent replacement but are expensive to machine. Laser-aided DED system consists of a powder feed nozzle on a multi-axis table, which deposits materials melted by the laser beam on the target surface, where it solidifies [3]. DED process can print a wide variety of metals including Titanium [4, 5], Nickel- and Cobalt-based superalloys [6–8], Tool steels [9, 10] – all of which are commercially available, and customized materials by mixing powders with

specified composition ratio [11]. Besides, with optimized parameters, the process can precisely deposit materials in a specified area with a small heat affected zone, enabling remanufacturing of fine thin-wall structures [12, 13]. Moreover, the metallurgical bond can be formed between deposits and substrates to guarantee excellent interfacial adhesion strength [14]. All these specialties make DED process for component repair a research hotspot. A multi-axis laser deposition process has the capability of depositing materials onto the damaged parts to restore them to the near net-shaped parts. The multi-axis hybrid manufacturing process, which integrates the machining process and the direct laser deposition process on a single workstation such as a CNC machine, can restore a damaged part to the machined quality without post-processing. This process could also be a robotic deposition process which can repair damaged structures or machines in the field.

A DLD process is often used to build a 3-D part layer by layer, in which material is often injected on a relatively flat surface. The process planner or controller for such additive applications is based on parallel slicing information. However, for a damaged part, the geometric shape is unpredictable and usually is not a flat surface; thus, traditional algorithms in layered manufacturing are not suitable for remanufacturing. Another challenge in remanufacturing is to automatically identify the damaged portion of the part. To fully automate the remanufacturing process, an effective process planner to drive the remanufacturing process is greatly needed. This paper is to report on the research and development of a remanufacturing system tailored for an automatic DLD-based remanufacturing process.

Model Reconstruction

In order to reconstruct damaged geometry, it is necessary to recreate the model of a worn part using scanners. Model of the nominal part can be regenerated by scanning the original part or from the CAD database. In this study, models of objects were recreated using a structured light metrology 3D scanner that can reach an accuracy of 25 µm (OptimScan 5M from Shining 3D Co., Fig. 1a). Structured light scanners project a narrow pattern of parallel stripes onto a three-dimensional object and convert distortions into 3D coordinates of a point cloud.

The scanning process is illustrated in Fig. 1b. To begin with, the scanner was calibrated and focused. After that, the prepared object is located on a table with indexing dots so that data from multiple scanning steps can be registered into a single model. The output is point cloud and can be post-processed to STL model. One can see that, although the scanning step is speedy, it still needs lots of manual intervention, especially in the scanning of complex objects where more scanning steps are required to capture all surfaces. To automate the process, a scanning configuration assisted by a 6-axis robot (NACHI SC300F-02) with an accuracy above ±0.5 mm was proposed as shown in Fig. 2. In the process, an object is clamped on the robot end-effector. The scanner is fixed while the position of the end-effector is precisely manipulated in the view of the 3D scanner cameras so that all surfaces of the object can be captured. The robot eliminates the time-consuming process of manually turning the object to find appropriate angles to capture all surfaces. It should be noted that the robot accuracy has no effects on the scanning accuracy as the robot just positioned the part and calibration points are attached on the object.

A model is used to assess the configuration to find general scanning procedures and common problems (Fig. 3a). The test model was designed in OpenSCAD and printed on the Stratasys uPrint SE plus FDM 3D printer. The dimensions of the model are 120 mm × 23.24 mm × 49.41 mm. The model was designed with features to simulate common scenarios.

(1) Cone: to test the ability to generate accurate point cloud at fine tips and curved surfaces of conical geometries.
(2) Sphere: to test the ability to scan points at the boundary of the sphere and the base.
(3) Stairs: to test the ability to scan depth accurately and fine edges of stairs.
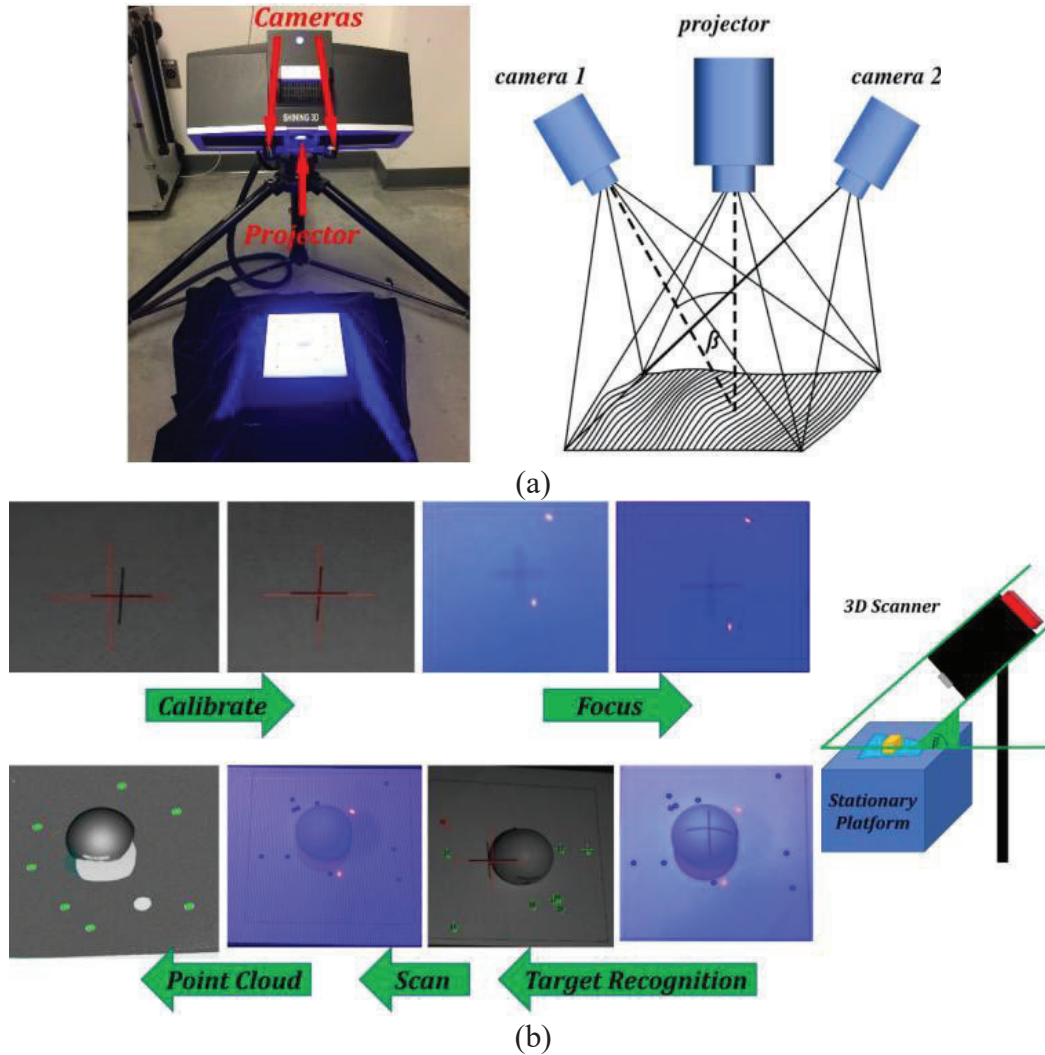(4) Cylinder: the bowl in the top is to test the ability to scan an object with interreflections.

Fig. 1 (a) OptimScan 5M 3D scanner; (b) and general scanning procedure.

Eighteen scans were taken at identical angles for the first five-axis of the robot but with rotating the end-effector with an increment of 20°. Using the robot to adjust the orientation of the object allows the part to be scanned entirely, without the cumbersome steps of altering the scanner

head angles. The scanned point cloud is shown in Fig. 3d. After scanning, there are still missing points between closely spaced objects, especially on sides of the stairs and underneath the sphere. The missing points are likely due to both cameras not being able to see the shapes at the same time.
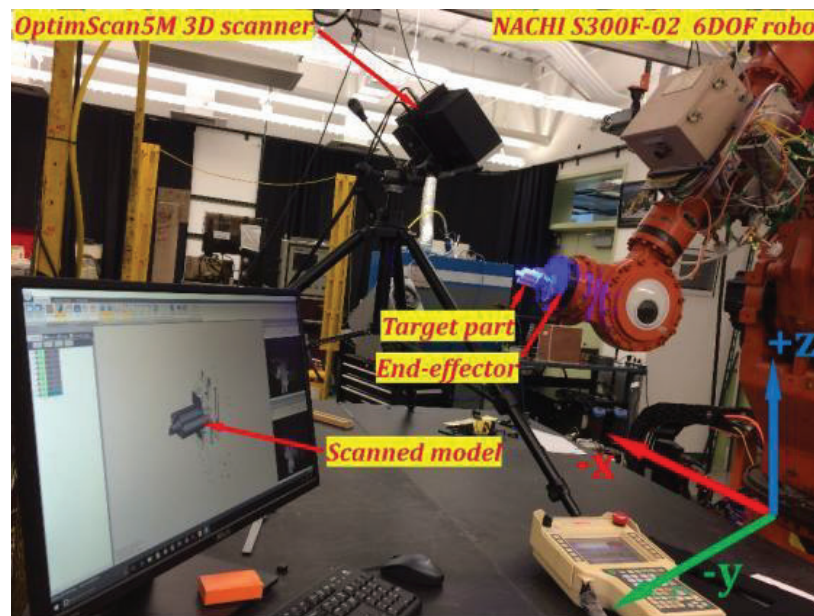

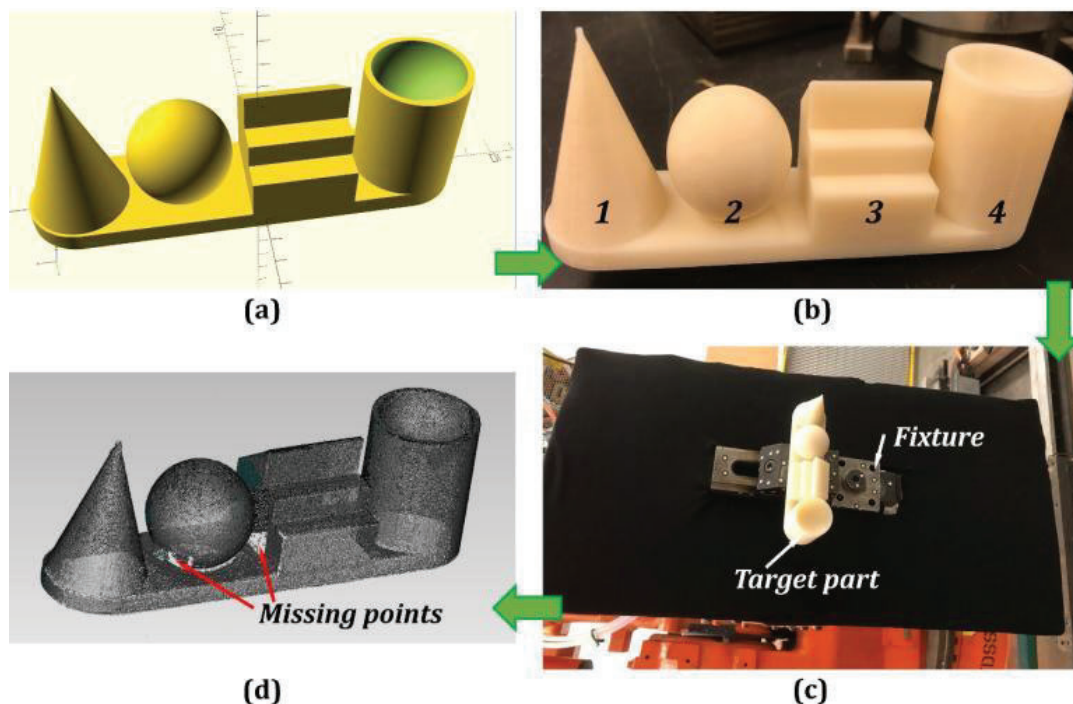**Fig. 2** The NACHI robot and 3D scanner setup

Fig. 3 Evaluation of the robot-assisted part scanning process: (a) 3D model designed in OpenSCAD; (b) 3D printed ABS plastic part; (c) Part clamped to NACHI end-effector; (d) A complete scan of the test model

Damage Reconstruction

The flowchart of the proposed damaged reconstruction algorithm is illustrated in Fig. 4, which includes the following eight steps:

Step 1: Import the aligned damaged and nominal STL models for processing.
Step 2: Select an area that covers the damaged geometry. Computing intersections of casting rays with the entire model is very time-consuming, especially for 3D scanned models because of numerous small facets. Reducing grid interval δ to improve accuracy will also increase computing time significantly. Therefore, by selecting the area that covers the damage, the damage reconstruction process can be accelerated.
Step 3: Compute the minimum bounding box of the selected area.
Step 4: Slice the minimum bounding box into grids according to a user-defined grid interval δ. Three initial casting rays along x-, y- and z-axis were created, respectively.
Step 5: Calculate intersections of the casting rays in three orthogonal directions with the nominal and damaged models.
Step 6: The quantity and values of intersections from the nominal and damaged models were compared. Based on the comparison, points in the damaged region were extracted.
Step 7: The extracted point set was output.
Step 8: After the above steps, the X, Y, and Z coordinates were updated according to the grid interval to generate the next casting rays to intersect the nominal and damaged models.

The above steps continue until the casting rays reach the boundary of the minimum bounding box. The extracted points form the damaged areas that need to be rebuilt.

Step 6 in the above flowchart is crucial to extract points in the damaged zone. The method for determining such points was illustrated as follows: As shown in Fig. 5a, $P\left(x_p, y_p, z_p\right)$ and $Q\left(x_q, y_q, z_q\right)$ are intersections of a ray with the nominal model. In general, there are two situations of the intersections between nominal and damaged models: (1) Identical intersection quantity but different values as shown in Fig. 5b. This situation can be taken place by partial fracture such as hole fracture shown in Fig. 5b. (2) Different intersection quantity as shown in Figs. 5c and 5d. In Fig. 5c, the inner hole is fractured, and some materials are missing. Therefore, no intersections will be obtained from casting ray with the damaged model. In Fig. 5d, a slot was created inside the hole, resulting in four intersections (P''', M, N, Q''') of the casting ray with the damaged model.

Based on the two scenarios, points enveloping the damaged region are extracted as follows: First, the quantity of the intersections of a casting ray with the nominal model and damaged model was compared. If the quantity was identical, coordinates of each point from the nominal model were compared with the coordinates of the point from the damaged model, e.g., $P(x_p, y_p, z_p)$ compared with $P'\left(x_{p'}, y_{p'}, z_{p'}\right)$, $Q\left(x_q, y_q, z_q\right)$ compared with $Q'\left(x_{q'}, y_{q'}, z_{q'}\right)$. Points with coordinates that beyond an acceptable tolerance were extracted, such as $Q\left(x_q, y_q, z_q\right)$ and

$Q'\left(x_{q'}, y_{q'}, z_{q'}\right)$. However, if the quantity of intersections is different and if there are no intersections of a ray with the damaged model (Fig. 5c), the intersections of the ray with the nominal model are extracted, such as $P(x_p, y_p, z_p)$ and $Q\left(x_q, y_q, z_q\right)$. If the quantity of intersections is different and there are intersections of the ray with the damaged model (Fig. 5d), a set difference between the intersections from the nominal model and intersections from the damaged model is conducted. The set difference operation will extract the points that envelope the damage, such as $M\left(x_m, y_m, z_m\right)$ and $N\left(x_n, y_n, z_n\right)$.

Fig. 6 depicts the damage reconstruction process using tri-dexel data for the die part. Fig. 6a shows the selected area for damage extraction. The intersections of casting rays with the selected region of nominal and damaged models were shown in Fig. 6b. The grid interval is 0.2 mm. The points that enveloping damaged zone were extracted are shown in Fig. 6c. The STL model of the damage was reconstructed using the Screened Poisson Surface Reconstruction with reconstruction depth of 10 (Fig. 6d) [15].
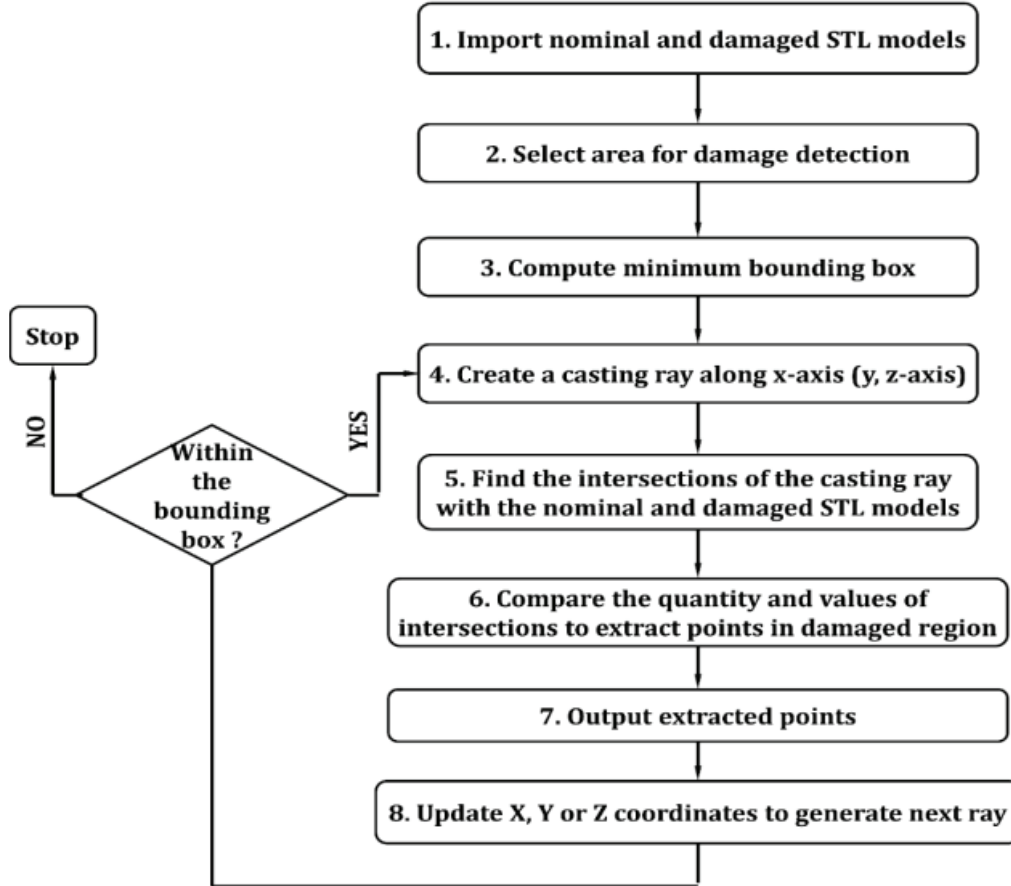

Fig. 4 Flowchart of the damage reconstruction process from tri-dexel data
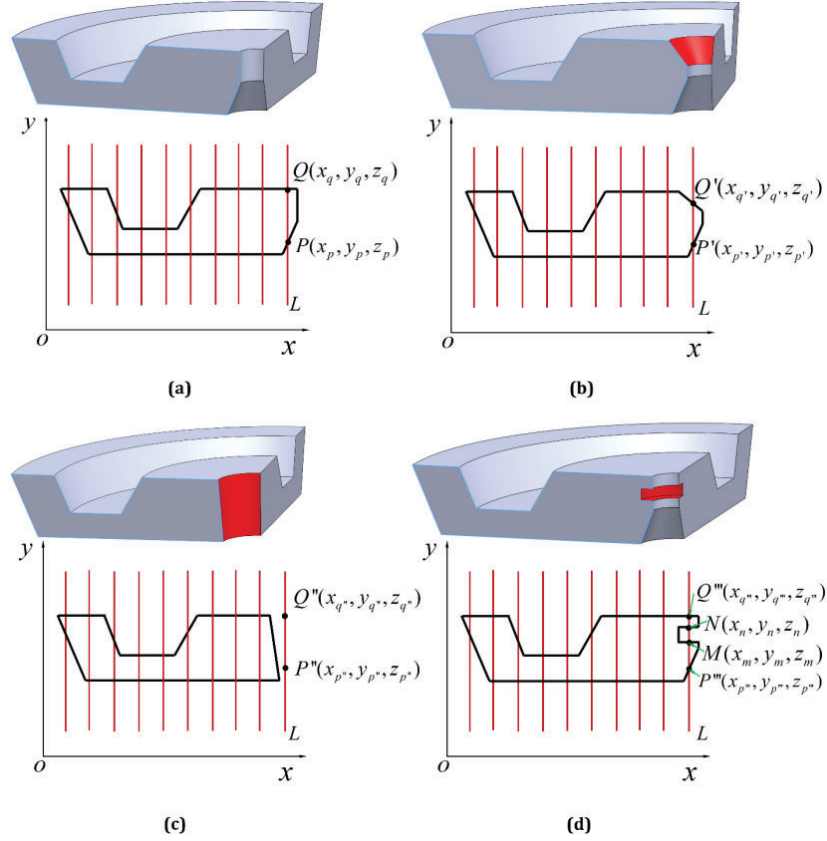
Fig. 5 Damage extraction. (a) Intersections of casting rays with the nominal model; Intersections of casting rays with the damaged model with hole boundary fracture (b), inner hole penetrating fracture (c) and the inner hole inside fracture (d)
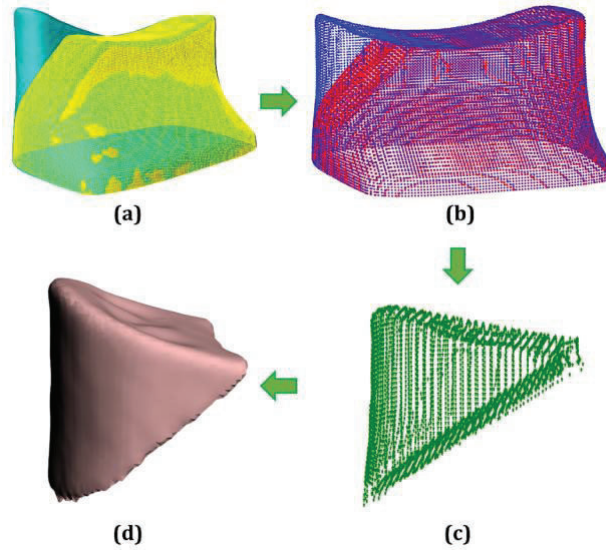

Fig. 6 Damage reconstruction for a fractured die. (a) Selected area for damage extraction; (b) Intersections of casting rays with the selected area of nominal and damaged models; (c) Extracted points; (d) STL model of the damage

Tool Path Generation

Three types of tool path were employed in this study, namely Helix (H), Circle-Line-Circle (CLC), and Line-Arc-Line (LAL), as shown in Fig. 7. The axial length of each tool path was designed to be 10 mm. For the H tool path, the stepper motor shown in Fig. 8 rotated continuously and the linear motion along x-axis was also performed uninterruptedly. The combined motion results in the H tool path as shown in Fig. 7 (a). For the CLC tool path, the stepper motor shown in Fig. 8 rotated a complete circle, then a rapid linear movement was done, and another complete circular motion was followed. The rotation and linear motions were conducted alternately till the end point. Unlike the CLC route, for LAL path, a linear motion was done at first to move the laser beam from one end to another. After that, a rapid arc rotation was followed to rotate the substrate and a linear motion was then employed. Each tool path was carefully designed so that the overlap ratio between two adjacent tracks was the same, which is 0.5.

Wallex 40 coatings were fabricated on the moving substrate layer by layer. After each layer's deposition, the substrate moved to the original position and then moved 0.3 mm away from the laser beam and powder feed nozzle to conduct the next layer's cladding. A total of 5 layers were conducted using each type of tool path.
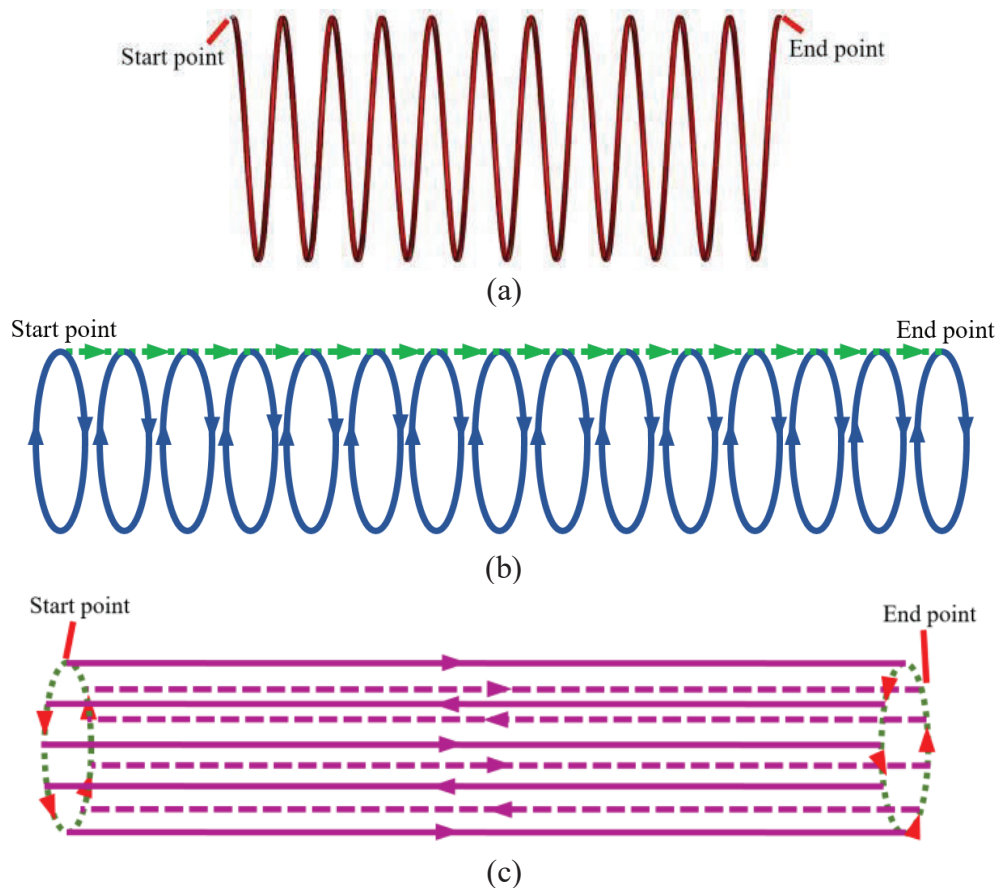

(a)

(b)

(c)

Fig. 7 Tool path generation; (a) Helix (H); (b) Circle-Line-Circle (CLC); (c) Line-Arc-Line (LAL)
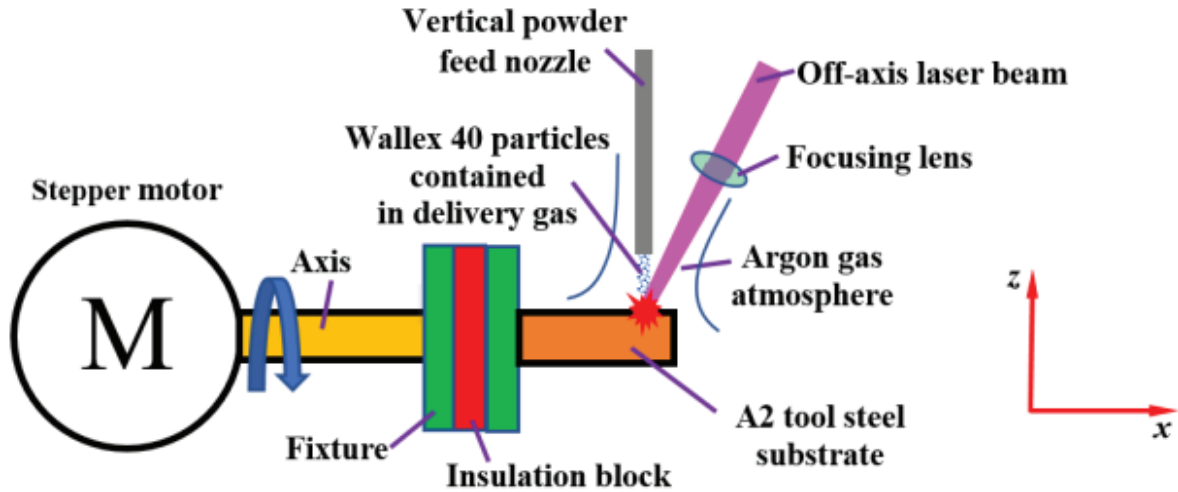
Fig. 8 Schematic diagram of the experimental set-up

Remanufacturing Process

In this study, the laser-aided DED process was conducted using a maximum 1 kW fiber laser from IPG Photonics, a commercial powder feeder from Bay State Surface Technologies, argon gas delivery unit, a designed off-axis powder feeding tube, and 3-axis motion table. Argon was also used as the shielding gas to avoid deposits from oxidation.

The material of the die is AISI H13 tool steel. To make sure the repaired sample will have better corrosion and abrasive resistance, Cobalt-based alloy Wallex 40 from Wall Colmonoy Limited (UK) was selected as the filler material. SEM micrograph and particle size distribution of Wallex 40 powder are depicted in Fig. 9. The average particle diameter was 71 μm. The chemical composition of Wallex 40 and H13 tool steel is listed in Table 1.
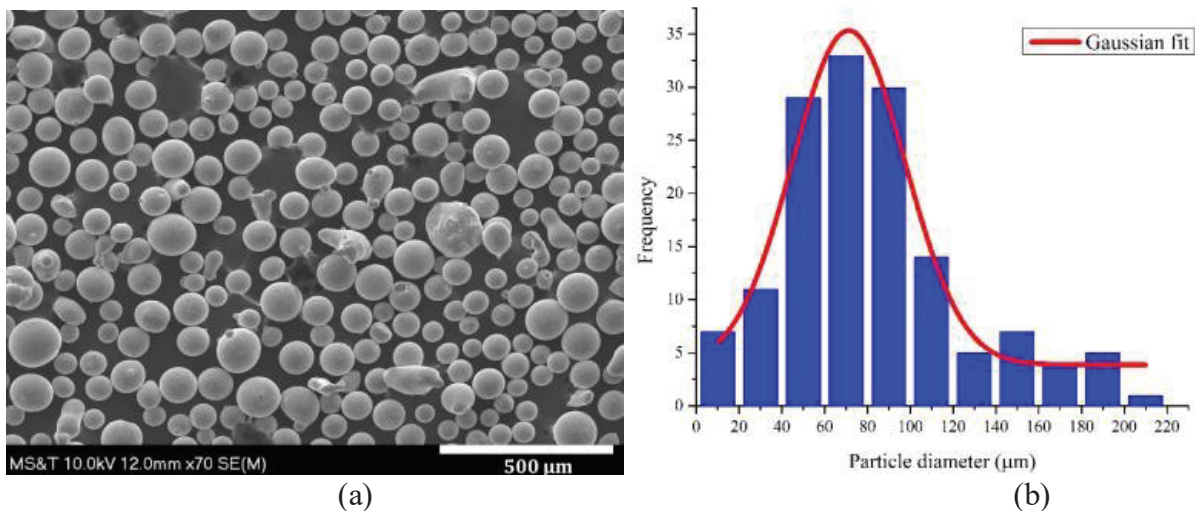

(a)   (b)

Fig. 9 (a) SEM micrograph of Wallex 40 powder; (b) Wallex 40 particle size distribution

Table 1 Chemical composition of the target materials (wt %)

Materials	C	Mn	Si	Cr	Ni	Mo	V	W	B	Fe	Co
H13 tool steel	0.4	0.4	1.0	5.25	-	1.35	1.0	-	-	Bal.	-
Wallex 40	0.6	-	1.9	16.2	23.5	-	-	7.6	2.0	1.3	Bal.

Results and Discussions

The reconstructed damage as shown in Fig. 10a was sliced into ten layers with a layer thickness of 0.5 mm. Then raster deposition tool path was generated as shown in Fig. 10b. Remanufacturing experiment was conducted according to the processing parameters listed in Table 2. Images of the repaired die are shown in Fig. 10c.

Table 2 Laser-aided DED processing parameters

Laser power (W)	Scan speed (mm/min)	Powder feed rate (g/min)	Layer thickness (mm)	Track overlap
600	220	4	0.5	0.5

(a)

(b)

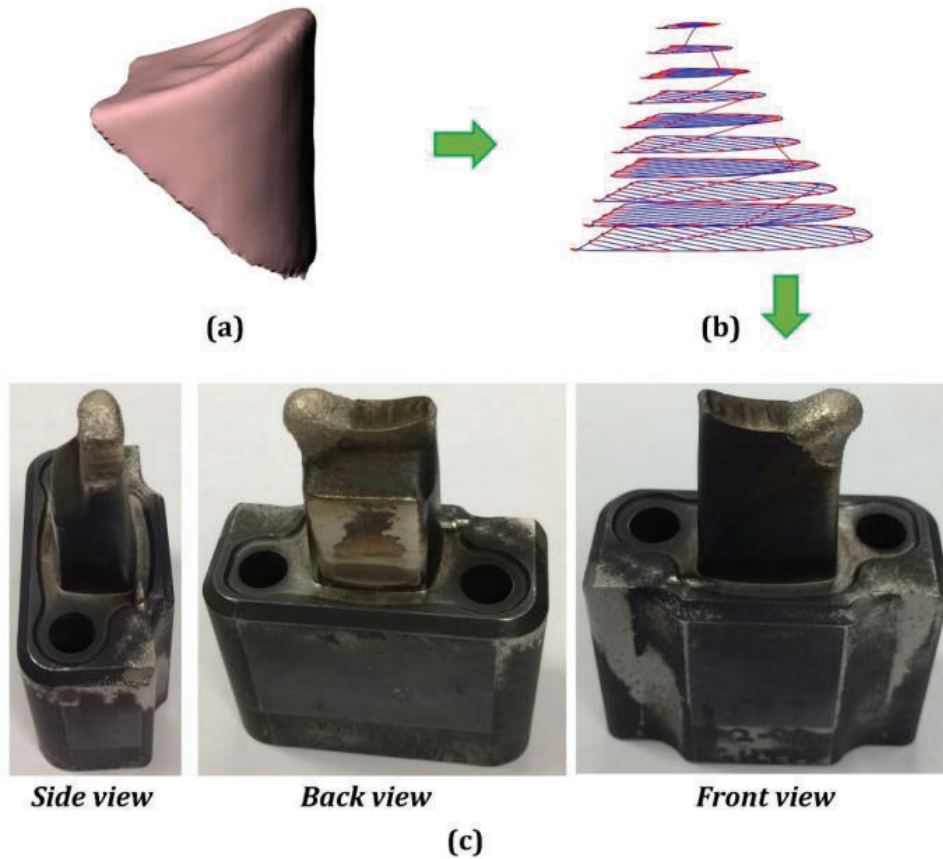Side view   Back view   Front view

(c)

Fig. 10 Tool path generation and repair result. (a) Reconstructed STL model of the damage; (b) Deposition tool path; (c) Die after material deposition

Two kinds of samples were prepared for the tensile test. In Fig. 11a, the sectioned tensile specimen consists of deposits and substrate material, with the interface located approximately in the middle of the tensile sample. In Fig. 11b, the tensile specimen was only made of as-deposited material. It was found that Wallex 40 is stronger than H13 from the as-deposited material tests. Tensile specimens were tested using Instron universal tester with a crosshead speed of 0.015 mm/min.
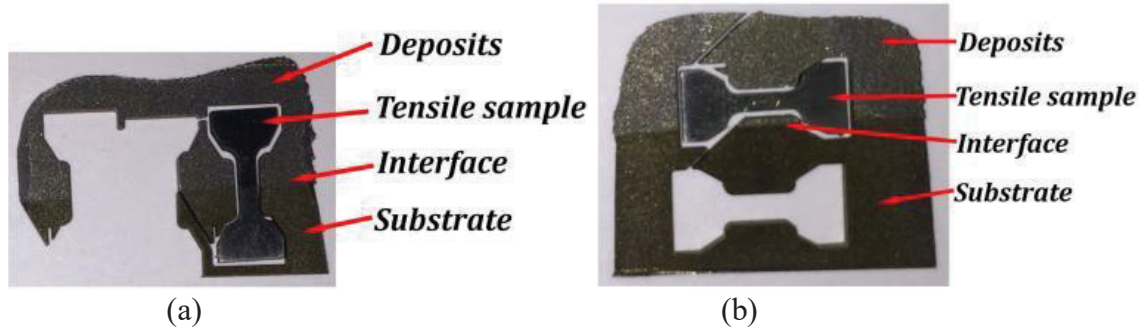

<div align="center">(a)   (b)</div>

Fig. 11 Tensile specimen preparation. (a) Tensile specimen made of Wallex 40 and H13 tool steel; (b) Tensile specimen made of Wallex 40

The stress-strain curves obtained from tensile testing are shown in Fig. 12. The tensile testing of combined samples (Wallex 40 + H13 tool steel) shown in Fig. 12 revealed largely consistent tensile properties. H13 steel was used as the substrate. All specimens were broken at the H13 substrate portion since Wallex 40 is stronger than H13. The tensile stress increased with the increase of tensile strain to a peak of around 900 MPa. Then the tensile samples yield and finally fractured.
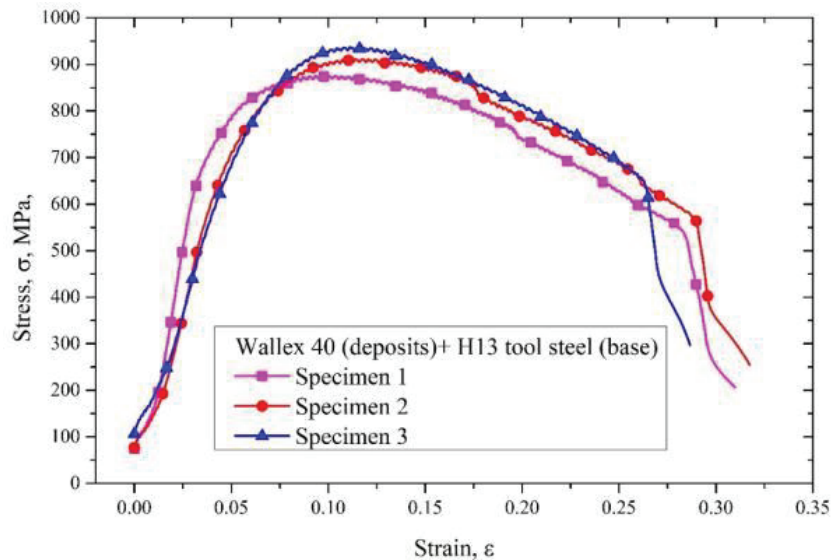

Fig. 12 Tensile stress-strain curves obtained from tensile test for Wallex 40 + H13 tool steel samples.

Conclusions

Automated remanufacturing metal parts is summarized in this study. Based on the shape and location of the damaged section and undamaged section, the different strategy can be selected to balance the remanufacturing feasibility and efficiency. A scanning routine was determined by scanning a designed part with general features. The integration of the 6DOF industrial robot with 3D structured light scanner benefits the scanning process by eliminating the time-consuming process of manually turning the object to find appropriate angles to capture all surfaces. Reconstructed damage from tri-dexel data was compared with the actual damage generated from CAD modeling, and the result shows by reducing the grid interval to 0.2 mm, the accuracy of reconstructed damage could reach up to ±0.1 mm, which is sufficient for remanufacturing purpose. STL model of the defective region was reconstructed through the extracted point cloud using Screened Poisson Surface Reconstruction algorithm. The damage reconstruction algorithm from tri-dexel data was evaluated in functionality and reliability by several illustrating examples. Extra material can be removed through high precise CNC machining. The remanufacturing experiments validate the feasibility of the remanufacturing strategies presented in this research.

Acknowledgments

References

[1]   Richter, Karl-Hermann; Orban, Sven and Nowotny, Steffen, (2004), "Laser Cladding of The Titanium Alloy Ti6242 of Restore Damaged Blades", Proceedings of the 23rd International Congress on Applications of Lasers and Electro-Optics 2004.

[2]   Penaranda X, Moralejo S, Lamikiz A, Figueras J (2017) An adaptive laser cladding methodology for blade tip repair. Int J Adv Manuf Technol 92:4337–4343. doi: 10.1007/s00170-017-0500-1

[3]   Mançanares CG, de S. Zancul E, da Silva J, Cauchick Miguel PA (2015) Additive manufacturing process selection based on parts' selection criteria. Int J Adv Manuf Technol 80:1007–1014. doi: 10.1007/s00170-015-7092-4

[4]   Baufeld B, Biest O Van der, Gault R (2010) Additive manufacturing of Ti–6Al–4V components by shaped metal deposition: Microstructure and mechanical properties. Mater Des 31:S106–S111. doi: 10.1016/j.matdes.2009.11.032

[5]   Dutta B, Froes FH (Sam) (2017) The Additive Manufacturing (AM) of titanium alloys. Met Powder Rep 72:96–106. doi: https://doi.org/10.1016/j.mprp.2016.12.062

[6]   Dinda GP, Dasgupta AK, Mazumder J (2009) Laser aided direct metal deposition of Inconel 625 superalloy: Microstructural evolution and thermal stability. Mater Sci Eng A 509:98–104. doi: https://doi.org/10.1016/j.msea.2009.01.009

[7]   Jia Q, Gu D (2014) Selective laser melting additive manufacturing of Inconel 718 superalloy parts: Densification, microstructure and properties. J Alloys Compd 585:713–721. doi: https://doi.org/10.1016/j.jallcom.2013.09.171

[8]   Lin WC, Chen C (2006) Characteristics of thin surface layers of cobalt-based alloys

deposited by laser cladding. Surf Coatings Technol 200:4557–4563. doi: 10.1016/j.surfcoat.2005.03.033

[9] Imran MK, Masood SH, Brandt M, et al (2011) Direct metal deposition (DMD) of H13 tool steel on copper alloy substrate: Evaluation of mechanical properties. Mater Sci Eng A 528:3342–3349. doi: https://doi.org/10.1016/j.msea.2010.12.099

[10] Bhattacharya S, Dinda GP, Dasgupta AK, Mazumder J (2011) Microstructural evolution of AISI 4340 steel during Direct Metal Deposition process. Mater Sci Eng A 528:2309–2318. doi: https://doi.org/10.1016/j.msea.2010.11.036

[11] Li W, Chen X, Yan L, et al (2017) Additive manufacturing of a new Fe-Cr-Ni alloy with gradually changing compositions with elemental powder mixes and thermodynamic calculation. Int J Adv Manuf Technol. doi: 10.1007/s00170-017-1302-1

[12] Kumar S, Sharma V, Choudhary AKS, et al (2013) Determination of layer thickness in direct metal deposition using dimensional analysis. Int J Adv Manuf Technol 67:2681–2687. doi: 10.1007/s00170-012-4683-1

[13] Shamsaei N, Yadollahi A, Bian L, Thompson SM (2015) An overview of Direct Laser Deposition for additive manufacturing; Part II: Mechanical behavior, process parameter optimization and control. Addit Manuf 8:12–35. doi: https://doi.org/10.1016/j.addma.2015.07.002

[14] Wang Z, Guan K, Gao M, et al (2012) The microstructure and mechanical properties of deposited-IN718 by selective laser melting. J Alloys Compd 513:518–523. doi: https://doi.org/10.1016/j.jallcom.2011.10.107

[15] Zhang, Xinchang, Wei Li, Kate Adkison, Frank Liou, "Damage Reconstruction from Tridexel Data for Laser-aided Repairing of Metallic Components," The International Journal of Advanced Manufacturing Technology, March 2018